Received: 5 May 2025 | Revised: 18 July 2025 | Accepted: 30 July 2025

DOI: 10.1002/pro.70265

RESEARCH ARTICLE

THE PROTEIN SOCIETY WILEY

Structural insight into the substrate binding of the AMT complex via an inhibitor-trapped state

Zengyu Shao[1] | **Sol Yoon**[1] | **Jiuwei Lu**[1] | **Pranav Athavale**[1] | **Yifan Liu**[2] | **Jikui Song**[1]

[1]Department of Biochemistry, University of California, Riverside, California, USA

[2]Department of Cancer Biology, University of Southern California, Los Angeles, California, USA

Correspondence
Jikui Song, Department of Biochemistry, University of California, Riverside, California 92521, USA.
Email: jikui.song@ucr.edu

Funding information
National Institutes of Health, Grant/Award Number: R35GM119721; National Science Foundation, Grant/Award Number: MCB-2435178

Review Editor: John Kuriyan

Abstract

N6-adenine (6mA) DNA methylation plays an important role in gene regulation and genome stability. The 6mA methylation in *Tetrahymena thermophila* is mainly mediated by the AMT complex, comprised of the AMT1, AMT7, AMTP1, and AMTP2 subunits. To date, how this complex assembles on the DNA substrate remains elusive. Here we report the structure of the AMT complex bound to the OCR protein from bacteriophage T7, mimicking the AMT–DNA encounter complex. The AMT1–AMT7 heterodimer approaches OCR from one side, while the AMTP1 N-terminal domain, assuming a homeodomain fold, binds to OCR from the other side, resulting in a saddle-shaped architecture reminiscent of what was observed for prokaryotic 6mA writers. Mutation of the AMT1, AMT7, and AMTP1 residues on the OCR-contact points led to impaired DNA methylation activity to various extents, supporting a role for these residues in DNA binding. Furthermore, structural comparison of the AMT1–AMT7 subunits with the evolutionarily related METTL3–METTL14 and AMT1–AMT6 complexes reveals sequence conservation and divergence in the region corresponding to the OCR-binding site, shedding light on the substrate binding of the latter two complexes. Together, this study supports a model in which the AMT complex undergoes a substrate binding-induced open-to-closed conformational transition, with implications in its substrate binding and processive 6mA methylation.

KEYWORDS
6mA DNA methylation, AMT complex, DNA methyltransferase, enzyme–substrate recognition, homeodomain, maintenance DNA methylation, open-to-close conformational transition, protein–DNA interaction

1 | INTRODUCTION

DNA methylation is an epigenetic mechanism critically influencing chromatin structure and function. The most well-known DNA methylation occurs at the C-5 position of cytosines, which functions to regulate gene expression (Bird & Wolffe, 1999; Razin & Riggs, 1980), X-chromosome inactivation (Panning & Jaenisch, 1998), transposon silencing (Bourc'his & Bestor, 2004; Walsh et al., 1998), and genome stability (Jones & Gonzalgo, 1997). In addition, DNA methylation at N6-adenine (6mA) plays a role in modulating genome function in both prokaryotes and eukaryotes (Boulias & Greer, 2022; Luo et al., 2015). Recent studies have further linked 6mA DNA methylation in protists, green algae, and basal fungi, occurring predominantly in the context of ApT dinucleotides, to epigenetic regulation due to its association with transcriptionally active domains (Beh et al., 2019; Fu et al., 2015; Mondo et al., 2017; Wang et al., 2019) and epigenetic marks H2A.Z and H3K4me3 (Sheng et al., 2024; Wang et al., 2025). However, in contrast to the writers of C-5 DNA methylation that have been well characterized (Cheng, 1995a; Du et al., 2015; Law & Jacobsen, 2010;

Ren et al., 2018; Song & Pfeifer, 2016; Zhang et al., 2023), the structure and mechanism of the writers for 6mA DNA methylation in eukaryotes remain elusive.

In unicellular eukaryote *Tetrahymena thermophila*, 6mA DNA methylation is mainly maintained by the highly processive AMT complex comprised of AMT1 methyltransferase (MTase) and regulatory subunits AMT7, AMTP1, and AMTP2 (a.k.a. MTA1, MTA9, p1 and p2, respectively, in the same organism) (Beh et al., 2019; Wang et al., 2019). In addition, a variant of the AMT complex, in which AMT7 is replaced by a shorter homologue AMT6, plays a role in the maintenance of 6mA methylation in a replication-coupled manner (Wang et al., 2025). Previous structural and biochemical characterizations of the AMT complex reveal that AMT1, AMT7, AMTP1, and AMTP2 form a heterotetramer in a stoichiometry of 1:1:1:1 (Chen et al., 2022; Yan et al., 2023). Among these, the catalytic AMT1 subunit harbors a classic DPPW catalytic motif, stacked with the regulatory AMT7 subunit in a manner resembling the heterodimeric RNA adenine methyltransferase METTL3–METTL14 complex (Sledz & Jinek, 2016; Wang, Doxtader, & Nam, 2016; Wang, Feng, et al., 2016). Furthermore, a long N-terminal helix of AMT1 bridges the AMT1–AMT7 heterodimer with the AMTP1 and AMTP2 subunits through interactions with AMTP2 and the C-terminal helix (CH) of AMTP1. It has been established that the AMT complex-mediated 6mA methylation requires the presence of all four subunits, with the homeodomain-like DNA-binding proteins AMTP1 and AMTP2 critically regulating substrate binding (Chen et al., 2022; Yan et al., 2023). However, due to a lack of structural information on substrate recognition, the molecular mechanism by which the four subunits of the AMT complex orchestrate 6mA methylation remains elusive.

To elucidate the mechanism of the substrate binding by the AMT complex, we resorted to the Overcoming Classical Restriction (OCR) protein from bacteriophage T7, a mimic of B-form DNA (Putnam & Tainer, 2005), to stabilize the potential DNA-binding surfaces of AMT1, AMT7, AMTP1, and AMTP2. The OCR protein binds to the AMT complex tightly, leading to inhibition of the latter's DNA methylation activity. On this basis, we solved the single-particle cryo-EM structure of the AMT1–AMT7–AMTP1–AMTP2–OCR complex. The cryo-EM structure of the AMT complex reveals saddle-shaped architecture, in which the AMT1–AMT7 heterodimer is bridged with the AMTP1 and AMTP2 subunits via the AMT1 N-terminal helix (NH). Strikingly, the AMT1–AMT7 subunits are joined by the N-terminal domain of AMTP1, which is otherwise structurally disordered in the apo form of the AMT complex, to flank the conformationally dynamic OCR, resulting in a closed conformation reminiscent of what was observed for many other 6mA writers in prokaryotes. Our combined structural and biochemical analysis confirmed the OCR-binding surface as potential DNA-binding sites and shed light on the substrate-binding mechanism of the evolutionarily related METTL3–METTL14 complex. Together, this study supports the notion that the AMT complex undergoes an open-to-closed conformational transition upon substrate binding, with important implications in the mechanism of the AMT complex-mediated 6mA DNA methylation.

2 | RESULTS

2.1 | The OCR protein inhibits the AMT complex-mediated 6mA DNA methylation

A previous structural study of the AMT complex, despite the presence of DNA substrate, failed to observe the density of the DNA (Yan et al., 2023), suggesting that the AMT–DNA association is highly dynamic. To overcome this challenge, we resorted to the OCR protein from T7 bacteriophage for stabilizing the substrate-binding conformation of the AMT complex (Figure 1a–c). OCR reportedly exists in a homodimeric form mimicking a slightly bent 20-base pair B-form DNA and has been shown to bind and inhibit DNA-templated enzymes (Issinger & Hausmann, 1972; Li et al., 2024; Walkinshaw et al., 2002). To test the interaction between the AMT complex and OCR, we performed size-exclusion chromatography analysis for the AMT complex and OCR, alone or in mixture. OCR co-migrated with the AMT complex on a Superdex 200 increase 10/300 GL column, indicative of stable association (Figures 1d,e and S1a,b). To evaluate whether the presence of OCR affects the AMT complex-mediated 6mA DNA methylation, we performed in vitro DNA methylation assay for the AMT complex on a 12-mer DNA duplex containing a single hemimethylated ApT site in the presence or absence of OCR. Consistent with previous observations (Beh et al., 2019; Chen et al., 2022; Sheng et al., 2024; Wang et al., 2019; Yan et al., 2023), the AMT complex is highly active on the hemimethylated ApT DNA (Figure 1f). However, the presence of OCR in a 2:1 molar excess reduced the DNA methylation efficiency of the AMT complex by ~100-fold (Figure 1f), indicative of strong inhibition. These data establish OCR as a DNA-mimicking inhibitor for the AMT complex-mediated 6mA DNA methylation.

2.2 | Structural overview of the OCR-bound AMT complex

Next, we solved the cryo-EM structure of the OCR-bound AMT complex at an 3.59-Å overall resolution (Figures 2a–d and S2 and Table S1). Structural analysis of the OCR-bound AMT complex reveals that the AMT complex is comprised of one copy of AMT1,

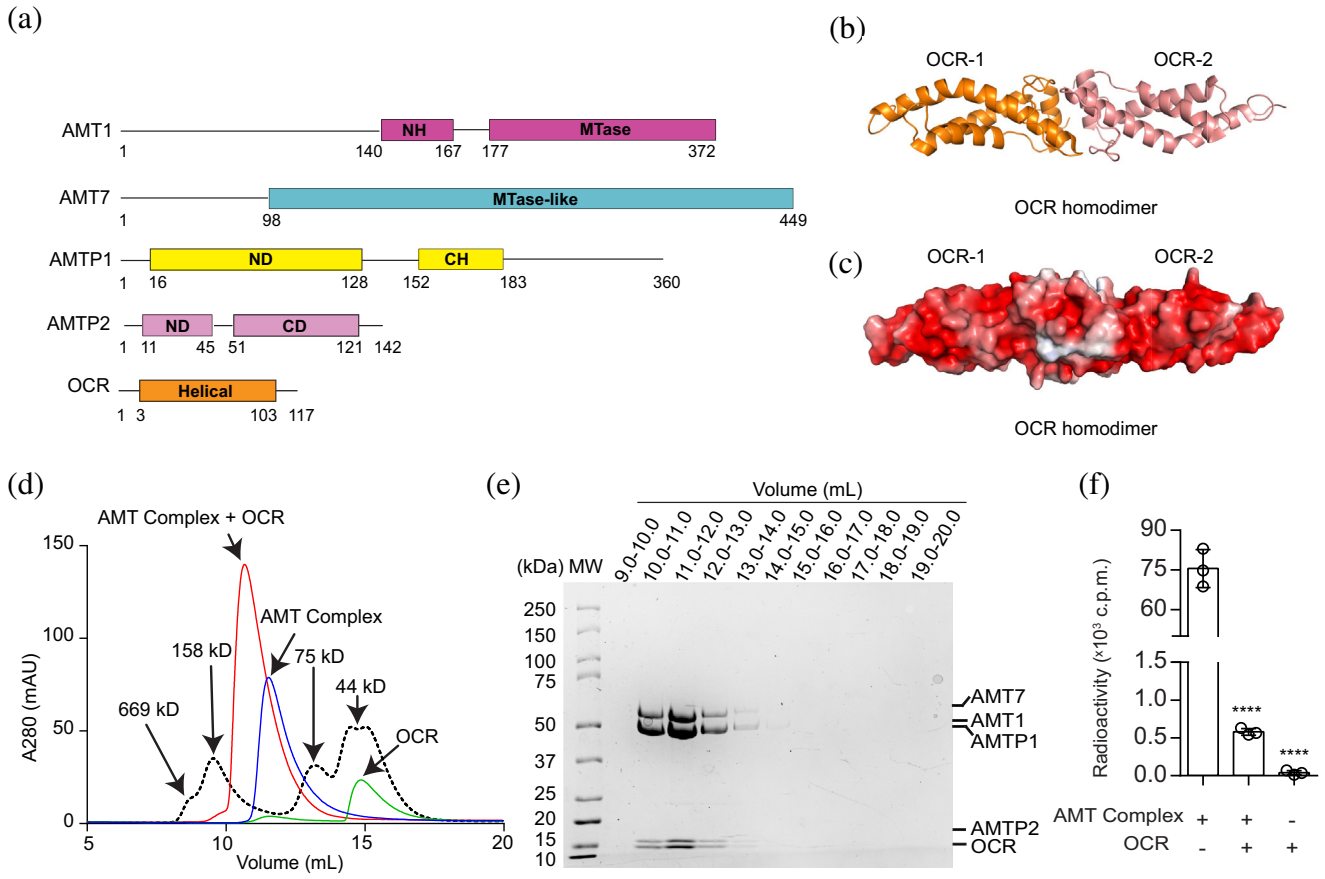

FIGURE 1 Biochemical analysis of the AMT–OCR complex. (a) Domain architecture of AMT1, AMT7, AMTP1, AMTP2, and OCR. CD, C-terminal domain; CH, C-terminal helix; ND, N-terminal domain; NH, N-terminal helix. (b, c) Ribbon (b) and surface electrostatic (c) representation of OCR homodimer (PDB 8ZEK). (d) Size-exclusion chromatography analysis of the AMT complex (blue), OCR (green), or AMT–OCR mixture (red). The elution profile for the molecular weight markers: thyroglobulin (669 kDa), aldolase (158 kDa), conalbumin (75 kDa), and ovalbumin (44 kDa) is shown as dashed line, with individual molecular weight indicated on top. (e) SDS-PGAE analysis of select fractions of the AMT–OCR mixture from size-exclusion chromatography in (d). (f) In vitro DNA methylation assay of the AMT complex on a hemimethylated 12-mer DNA duplex, in the presence or absence of OCR. Data are mean ± SD ($n = 3$ biological replicates). The two-tailed Student's t test statistical analysis was performed to compare the activity of AMT complex in the absence versus presence of OCR. ****$p < 0.0001$.

AMT7, AMTP1, and AMTP2 each (Figures 2a–d and S3a–i), consistent with previous observations (Chen et al., 2022; Yan et al., 2023). We were able to trace the density for AMT1 residues 128–216 and 227–372, AMT7 residues 99–114, 118–156, 162–228, 319–450, AMTP1 residues 16–128 and 154–184, and AMTP2 residues 11–132 (Figures 2c,d and S3a–i). The AMT1-bound S-adenosyl-homocysteine (SAH), by-product of the cofactor S-adenosyl-methionine (SAM), was also defined (Figure S3j).

The density for the OCR molecules bound to the AMT complex is rather weak and failed to be improved even after application of local refinement or focused classification, presumably due to conformational flexibility, which prevents us from accurate modeling (Figures 2a,b and S3e). Nevertheless, it is apparent that the OCR molecules are sandwiched by the N-terminal domain (ND) of AMTP1 from one side and the AMT1 MTase and AMT7 MTase-like domains on the other side (Figure 2a–d). As observed previously (Chen et al., 2022, Yan et al., 2023), the MTase domain of AMT1 associates with the MTase-like domain of AMT7 in antiparallel, resulting in a butterfly-like fold (Figure 2a–c). The AMTP1 protein is comprised of an N-terminal domain (ND) dominated by a helical fold and a structurally independent C-terminal helix (CH) (Figure 2a–c). The AMTP2 protein is comprised of an ND in a helix–loop–helix conformation and a C-terminal domain (CD) dominated by a four-helix bundle (Figure 2a–c). Notably, the AMT1 N-terminal helix (NH) engages in helical contacts with both the AMTP1 CH and the AMTP2 CD, thereby bridging the AMT1–AMT7 heterodimer with AMTP1 and AMTP2 (Figure 2a–d). Meanwhile, the ND of AMTP2 is docked onto the surface region formed by the beginning α-helix and β-strand, as well as the preceding loop, of the AMT1 MTase domain (Figure 2a–c).

Structural superposition of the OCR-bound AMT complex and the previously reported apo-form AMT complex (PDB 7YI8) (Yan et al., 2023) gave a

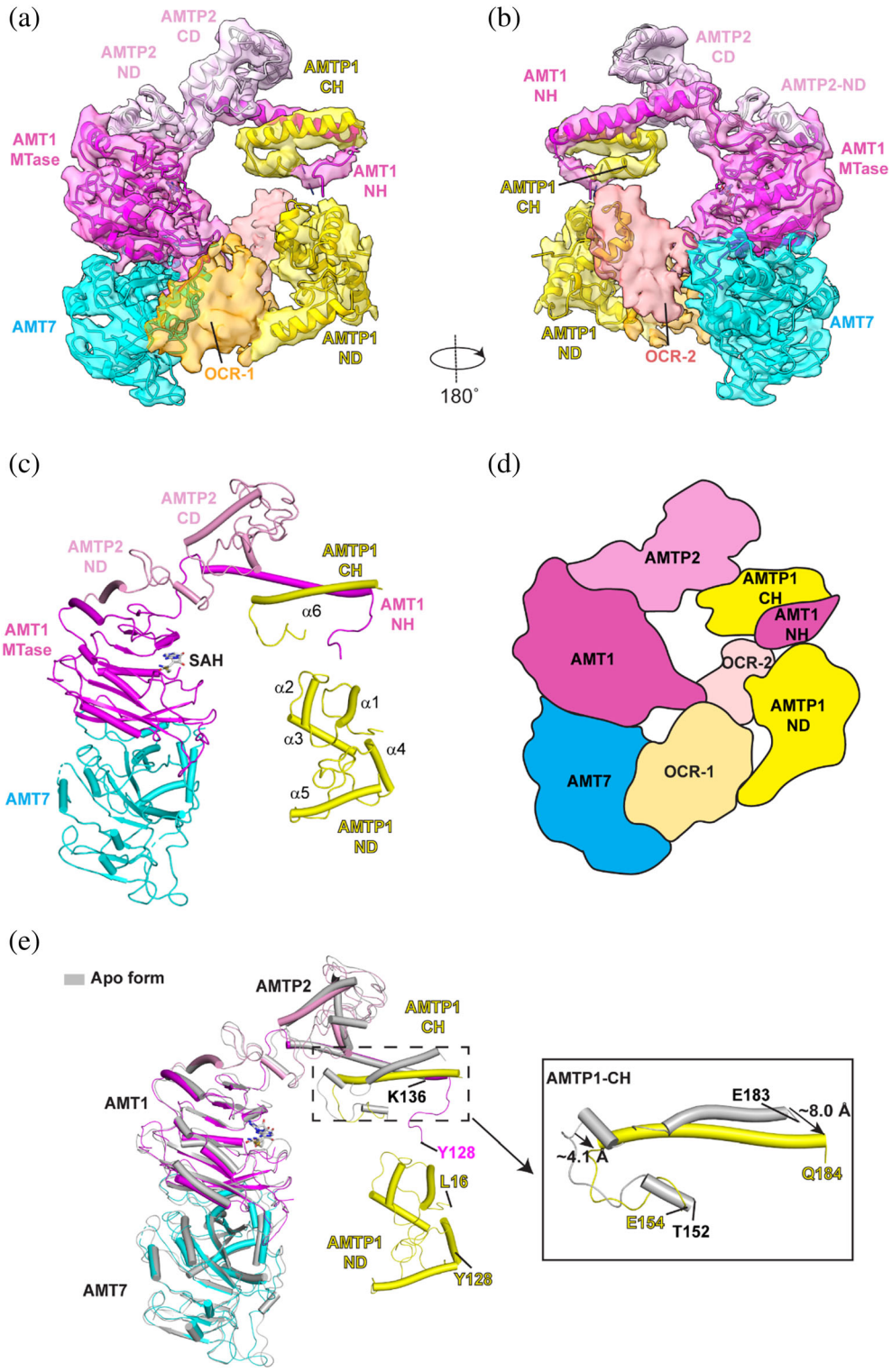

FIGURE 2 Cryo-EM structure of the OCR-bound AMT complex. (a, b) Two opposite views of the cryo-EM density map and atomic model of the AMT–OCR complex, with individual subunits and domains labeled. AMT1, AMT7, AMTP1, and AMTP2 are colored in magenta, cyan, yellow, and pink, respectively. The color scheme applies to subsequent figures unless otherwise indicated. The density corresponding to the OCR subunits (OCR-1 and OCR-2) are colored in orange and deep salmon, respectively. The atomic model for OCR dimer was not included in the final model due to its density being weak. (c) Atomic model of the AMT–OCR complex, with the cofactor by-product SAH molecule shown in stick representation. (d) Schematic view of the assembly of the AMT–OCR complex. (e) Structural overlay of apo-form (PDB 7YI8) and OCR-bound AMT complex, with the conformational shift for the AMTP1 CH highlighted in the expanded view. The N- and C-termini of the AMTP1 ND and the AMTP1 CH, and the N-terminus of AMT1 are indicated.

root-mean-square deviation (RMSD) of 1.2 Å over 531 aligned Cα atoms, indicative of high structural similarity (Figures 2e and S3k). The most notable difference between the two complexes lies in the AMTP1 ND domain, which is disordered in the apo-form AMT complex but is well defined in the OCR-bound form (Figures 2e and S3k), suggesting an OCR binding-induced structural stabilization effect. The conformational difference between the apo and OCR-bound AMT complex was further propagated to the AMTP1 CH (residues E154–Q184) (Figures 2e and S3k): upon the OCR binding, the N- and C-termini of the AMTP1 CH shifted toward the AMTP1 ND by ∼4 and ∼8 Å, respectively (Figures 2e and S3k).

2.3 | Mapping of the potential DNA-binding interface of the AMT complex

Analysis of surface electrostatic potential of the OCR-bound AMT complex reveals that the OCR molecules are walled by the positively charged surfaces of the AMT1 MTase domain, the AMT7 MTase-like domain, and the AMTP1 ND (Figure 3a–c). On one side, a cluster of residues at the AMT1–AMT7 interface, including AMT1 K280, K289, and H291 and AMT7 R379 and R382, forms a contact surface with the OCR (Figure 3b). Proximal to this surface are the residues (Y227, R357 and R358) around the SAH-binding site of AMT1, formed by two loop segments, namely Gate loops 1 and 2 (Chen et al., 2022; Yan et al., 2023) (Figure 3b). On the other side, AMTP1 residues K44, K46, K57, R68, K101, K114, and K118 form another contact surface for the OCR (Figure 3c).

The fact that the OCR protein serves as a mimic for the B-form DNA suggests that the OCR-contact sites of the AMT complex constitute its DNA-binding interface. To test this possibility, we selected the OCR-contact residues of AMT1, AMT7, and AMTP1 for mutagenesis and performed in vitro DNA methylation assays on substrates containing either a favorable hemimethylated ApT site or unfavorable, unmethylated ApT sites (Figure 3d–g). For the hemimethylated substrate, introducing the AMT1 K289A mutation led to a ∼3-fold reduction of the DNA methylation activity, while introducing the AMT1 Y227A, K280A, H291A, R357A, or R358A, or the AMT7 R379A or R382A mutation largely abolished the AMT activity (Figure 3d). Likewise, introducing the AMT1 and AMT7 mutations also led to a substantial reduction of the AMT activity on the unmethylated substrate (Figure 3e). For AMTP1, introducing the K57A and K101A mutations led to 2–4-fold lower methylation efficiency of the AMT complex on the hemimethylated substrate, and 3–6-fold lower methylation efficiency on the unmethylated substrate, suggesting an important role for these two sites in DNA binding (Figure 3f,g). On the other hand, a less pronounced effect was observed for the AMTP1 K44A, K46A, R68A, K114A, or K118A mutation, which led to slight or no activity change of the AMT complex on the hemimethylated substrate (Figure 3f). Nevertheless, it is apparent that these mutations significantly impair the AMT-mediated methylation on the less favorable, unmethylated substrates, supporting a role for these residues in fine-tuning the activity of the AMT complex (Figure 3g). Sequence analysis of AMT1, AMT7, and AMTP1 across various species further demonstrated that many of these potential DNA-binding sites, such as AMT1 Y227, K280, K289, H291, R357, and R358, AMT7 R379 and R382, and AMTP1 K44, K46, K57, R68, and K101, are evolutionarily conserved (Figures S4 and S5). Together, these data support the notion that the OCR-contact residues provide a DNA-binding interface underpinning the AMT-mediated 6mA DNA methylation.

2.4 | Comparative structural analysis of AMTP1 in AMT-mediated 6mA methylation

AMTP1 belongs to a broad family of homeodomains, which often interact with cognate DNAs to regulate cell- and tissue-specific gene expression (Burglin & Affolter, 2016). Through structural homology search using the DALI program (Holm & Rosenstrom, 2010), we identified a few structural homologues for AMTP1, including Double homeobox protein 4 (DUX4) (PDB 6E8C) (Lee et al., 2018), Myb-containing domain (MCD3) of double-strand telomeric DNA-binding proteins 2 (TEBP-2) (PDB 8U8L) (Padmanaban et al., 2024), Antennapedia homeodomain–DNA complex (PDB 9ANT) (Fraenkel & Pabo, 1998), and TEA domain family transcription factor 4 (TEAD4) (PDB 5GZB) (Shi et al., 2017) (Figure S6a). Notably, these proteins all harbor a homeodomain, employing a helix-turn-helix (HTH) motif to access the major groove of the DNA molecules (Figure S6b). It is worth noting that several OCR-contact sites of AMTP1 are also located on the corresponding region, spanning from α2-helix to α3-helix of the ND, such as K44, K46, K57, and R68, in addition to those from the neighboring β1-strand (K101) and α5-helix (K114 and K118) (Figures S5 and S6c). These data provide further insight into the DNA-binding sites of AMTP1.

2.5 | Structural comparison of the AMT complex with prokaryotic 6mA writers

To illustrate how the AMT complex-substrate binding is linked to prokaryotic adenine DNA methyltransferases, we generated a structural model of the AMT–DNA complex, based on the density corresponding to the OCR protein in the AMT–OCR complex. Due to the weak

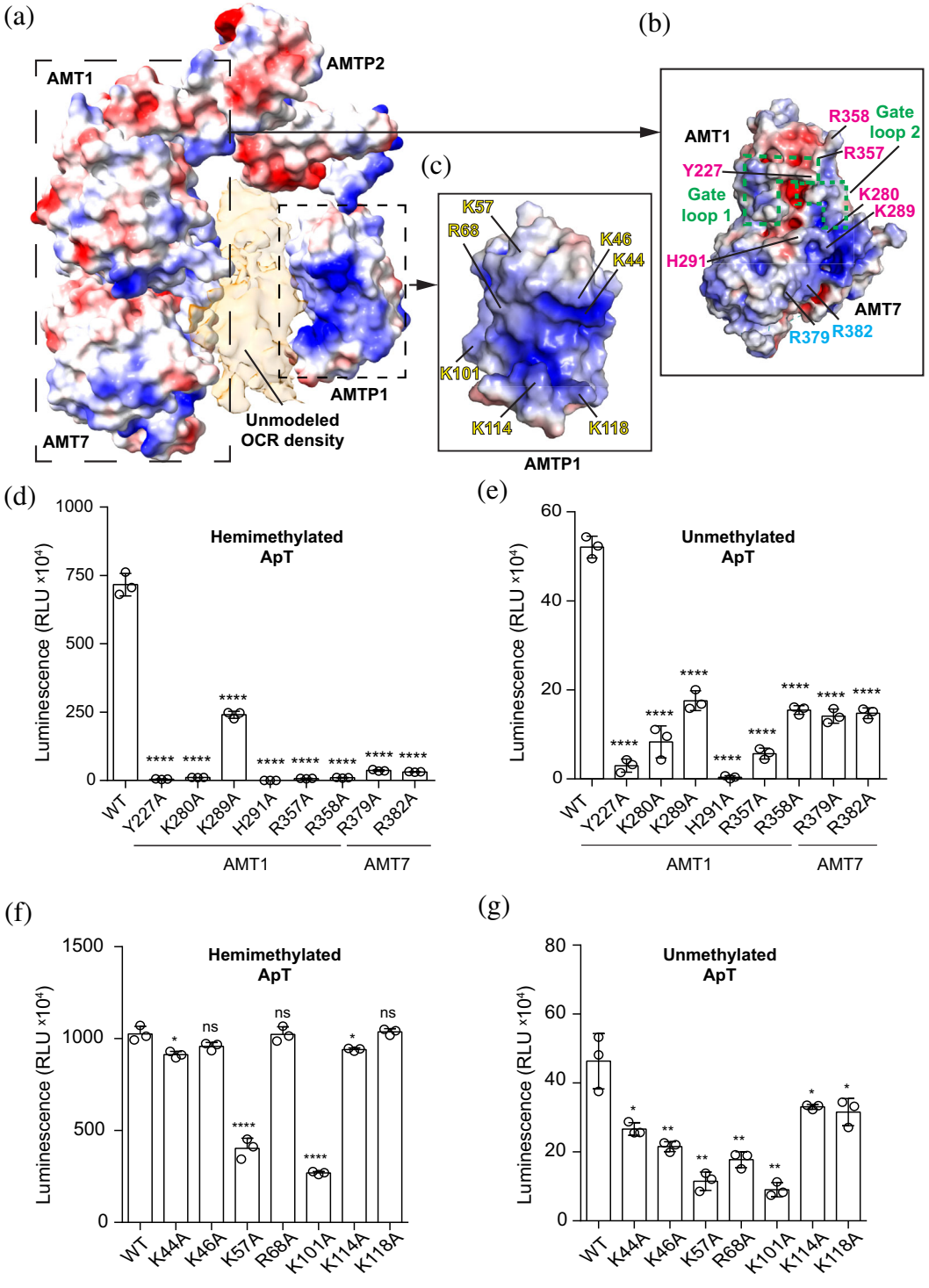

FIGURE 3 Structural and mutational analysis of the potential DNA-binding surface of the AMT complex. (a–c) Electrostatic surface of the AMT complex, with the entire surface shown in (a), and the potential substrate-binding sites of the AMT1–AMT7 dimer (b) and AMTP1 (c) shown in the expanded views. Gate loops 1 and 2 in AMT1 are highlighted by green dashed lines. (d, e) In vitro DNA methylation assay of the AMT1- or AMT7-mutated AMT complex on a hemimethylated 12-mer DNA duplex (d) or unmethylated 24-mer DNA duplex (e). Data are mean ± SD ($n = 3$ biological replicates). (f, g) In vitro DNA methylation assay of the AMTP1-mutated AMT complex on a hemimethylated 12-mer DNA duplex (f) or unmethylated 24-mer DNA duplex (g). Data are mean ± SD ($n = 3$ biological replicates). The two-tailed Student's *t* test statistical analysis was performed for pairwise comparison of the activity of WT versus mutant AMT complex. ns, not significant; *$p < 0.05$, **$p < 0.01$; ****$p < 0.0001$.

density of OCR, the DNA molecule was positioned in a random orientation. Nevertheless, the proximity between the DNA backbone and the AMTP1, AMT1, and AMT7 subunits agrees well with the AMT–OCR interactions (Figure 4a,b). We then performed a structural comparison of the AMT–DNA complex with

several prokaryotic 6mA writers, *E. coli* Type III restriction–modification enzyme EcoP15I-DNA complex (PDB 4ZCF) (Gupta et al., 2015), *Caulobacter crescentus* cell cycle-regulated DNA methyltransferase (CcrM)–DNA complex (PDB 6PBD) (Horton et al., 2019), and *Thermus aquaticus* DNA adenine methyltransferase M.TaqI–DNA complex (PDB 1G38) (Goedecke et al., 2001) (Figure 4c–h). Similar to the AMT complex, the EcoP15I complex employs multiple subunits for DNA binding, with the catalytic ModB subunit binding to the DNA from the minor groove and the target recognition domain (TRD) of the ModA subunit (TRD_A) binding to the major groove for sequence-specific recognition (Figure 4c,d). Likewise, the CcrM complex involves two copies of CcrM molecules for DNA binding, with one molecule approaching the minor groove for catalysis and the TRD from the other CcrM subunit (TRD′) approaching the major groove (Figure 4e,f). In contrast, the M.TaqI complex relies on two subdomains of M.TaqI: the catalytic core and the TRD, to bind DNA from the minor groove and major groove, respectively (Figure 4g,h). Despite the fact that these complexes employ distinct assembly mechanisms, they all form a deep cleft for processive DNA methylation (Figure 4a–h), highlighting similar yet distinct mechanisms of substrate DNA binding among the evolutionarily related 6mA DNA methyltransferases.

Structural comparison of the AMT complex with the prokaryotic 6mA writers further indicated that AMTP1 ND structurally corresponds to the major groove-binding components of the prokaryotic methyltransferase complexes, such as the TRD_A of the ModA subunit of EcoP15I, the TRD of the major groove-engaging CcrM molecule, and the TRD of M. TaqI (Figure S6d). Whether AMTP1 recognizes the target DNA in a similar manner to that of the TRD of the prokaryotic complexes warrants further investigation.

2.6 | Structural insights into the substrate-binding site of the METTL3–METTL14 complex

The AMT1–AMT7 heterodimer and the RNA adenine methyltransferase METTL3-METTL14 heterodimer belong to the same MT-A70 methyltransferase family (Beh et al., 2019; Wang et al., 2019), with high sequence and structural similarity (Chen et al., 2022; Wang, Doxtader, & Nam, 2016; Wang, Feng, et al., 2016; Yan et al., 2023). Structural overlay of the OCR-bound AMT complex with the METTL3–METTL14 complex (PDB 5IL1) (Wang, Feng, et al., 2016) reveals high structural similarity between the two complexes, with

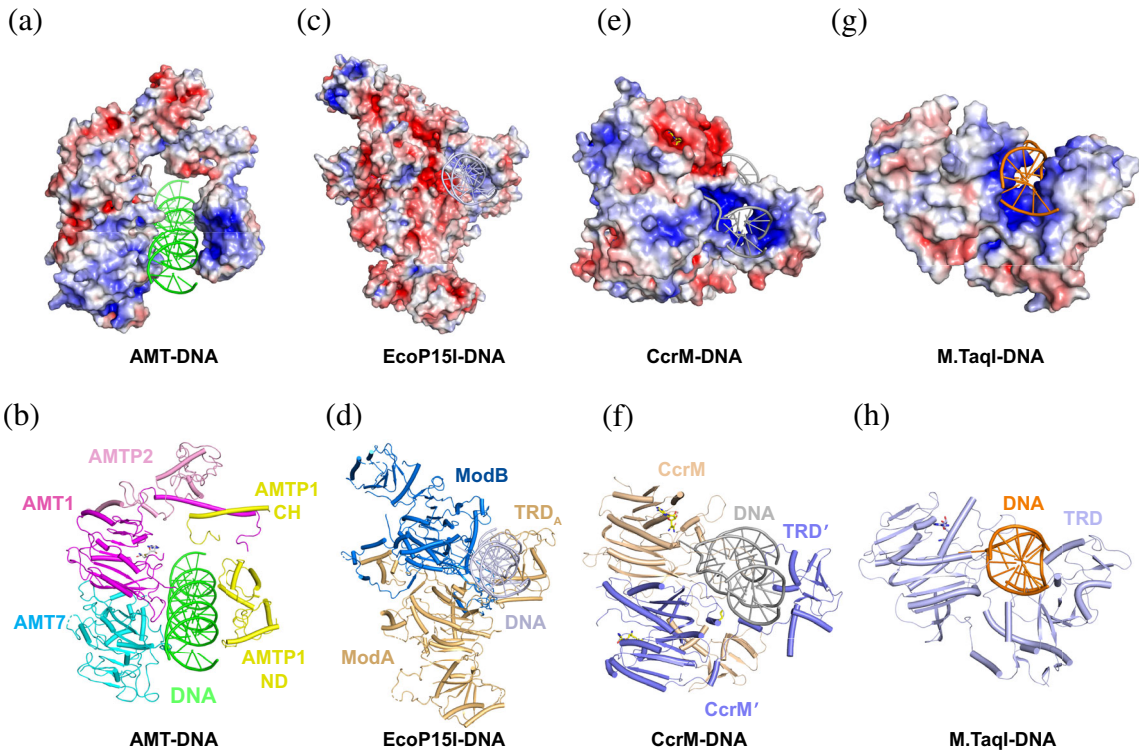

FIGURE 4 Structural comparison of the AMT–DNA model with the enzyme–substrate complexes of bacteria 6mA DNA methyltransferases. (a, b) Electrostatic surface (a) and ribbon representation (b) of the AMT–DNA model. (c, d) Electrostatic surface (c) and ribbon representation (d) of the EcoP15I Mod subunit-DNA (PDB 4ZCF). (e, f) Electrostatic surface (e) and ribbon representation (f) of the CcrM–DNA complex (PDB 6PBD). (g, h) Electrostatic surface (g) and ribbon representation (h) of the M.TaqI-DNA complex (PDB 1G38).

an RMSD of 1.13 Å over 161 aligned Cα atoms (Figure S7a). Notably, the SAM- and target adenosine-binding sites of the METTL3–METTL14 complex, formed by Gate loop 1 (METTL3 residues 396–410) and Gate loop 2 (METTL3 residues 507–515), are well aligned with the corresponding regions (residues 210–232 and 328–336, respectively) of AMT1 (Figure S7b). Furthermore, a number of DNA-binding sites of AMT1, such as residues Y227, K280, and R357, are conserved in METTL3 (Figure S7c), suggesting that AMT1 and METTL3 may employ a similar surface platform for substrate binding. On the other hand, the AMT7 residues R379/R382-corresponding sites in METTL14 are occluded from solvent access by two α-helices (Figure S7a), suggesting that they are unlikely to be involved in substrate binding in the METTL3–METTL14 complex. These observations shed light on the functional conservation and divergence between two evolutionarily related methyltransferases.

2.7 | Structural modeling analysis of the substrate binding by the AMT1–AMT6 complex

The AMT1–AMT6 complex, in which the AMT7 subunit in the AMT1–AMT7 complex is replaced by AMT6, is an alternative methyltransferase in maintaining the 6mA patterns shortly after DNA replication (Wang et al., 2025). With reduced methylation activity compared to the AMT1–AMT7 complex in vitro, the AMT1–AMT6 complex maintains the 6mA DNA methylation in cells in a proceeding cell nuclear antigen (PCNA)-dependent manner (Wang et al., 2025). To illustrate the substrate binding by the AMT1–AMT6 complex, we generated a structural model of the AMT1–AMT6 complex based on the structure of the AMT1–AMT7–AMTP1–AMTP2 complex and AlphaFold3 prediction (Abramson et al., 2024). The AMT1–AMT7 and AMT1–AMT6 complexes are structurally similar, with an RMSD of 1.77 Å over 1279 aligned Cα atoms (Figure S8a). Notably, the DNA-binding sites of AMT7, including R379 and R382, are also conserved in AMT6 (Figure S8b), suggesting a conserved DNA-binding mechanism between the two homologues. Nevertheless, AMT6 differs from AMT7 in the sequence of the disordered N-terminus (Figure S8b). In addition, the surface electrostatic potential of AMT6 appears less positively charged than that of AMT7, due to amino acid variation in the region near the DNA-binding site (Figure S8b–d). Whether such a difference in the DNA-binding site contributes to the differential methylation activity between the AMT1–AMT7 and AMT1–AMT6 complexes awaits further investigation.

3 | DISCUSSION

6mA DNA methylation in eukaryotes has gained increasing attention due to its functional implication in epigenetic regulation and genomic assembly (Feng & He, 2023). This study, through structure determination of an inhibitor-trapped state of the AMT complex from ciliated *Tetrahymena thermophila*, combined with enzymatic analysis, provides a framework for understanding how the AMT complex engages DNA substrate for 6mA maintenance methylation, with important implications in the functional regulation of 6mA DNA methylation in eukaryotes.

First of all, the structure of the AMT complex with the DNA-competitive inhibitor OCR supports a model that the AMT complex undergoes an open-to-closed conformational transition upon substrate binding (Figure 5). Previous structural characterization of the AMT complex reveals that, in the absence of DNA, AMT1, AMT7, AMTP2, and the C-terminal helix of AMTP1 adopt an open conformation, while the ND domain of AMTP1 is disordered (Chen et al., 2022; Yan et al., 2023). While these studies provide a framework for the functional assembly of the AMT complex, the lack of structural details for the ND domain of AMTP1 raises a question on its functional role in AMT-mediated 6mA DNA methylation. To overcome the challenge of the dynamic AMT–DNA interaction, we took advantage of a DNA-competitive inhibitor, the OCR protein, to stabilize the DNA-binding components of the AMT complex. As a result, we were able to capture a saddle-shaped architecture formed by AMT1, AMT7, AMTP1, and AMTP2, in which AMTP1 and the AMT1–AMT7 heterodimer coordinately flank the OCR protein. Consistently, our in vitro enzymatic analysis reveals that mutations of the putative DNA-binding sites of AMT1, AMT7, and AMTP1 impact AMT activity to various extents. Our comparative structural analysis further demonstrated that the ND domain of AMTP1 shares a

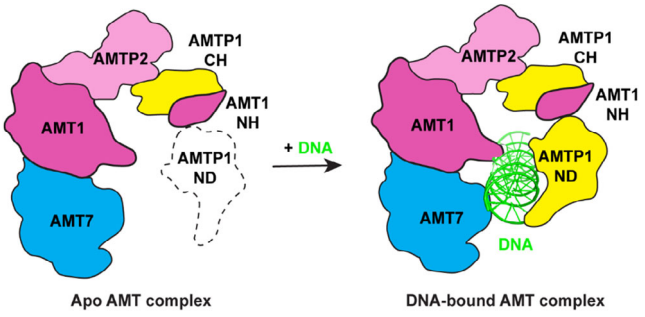

FIGURE 5 A working model of the AMT complex. In the absence of DNA substrate, the AMTP1 N-terminal domain is dynamically disordered, resulting in an open conformation. In the presence of DNA substrate, the AMT1–AMT7 dimer and the AMTP1 ND close up on DNA for methylation.

similar functional site with other members of the homeodomain family, implying a role for this domain to target the major groove of the DNA substrate. Whether AMTP1 contributes to the DNA sequence specificity of the AMT complex, as was observed for the TRD domain of a C-5 DNA methyltransferase (Cheng, 1995b; Ren et al., 2018), has yet to be elucidated.

It has been well known that DNA-templated enzymes often adopt a ring or saddle-shaped structure to process DNA (Breyer & Matthews, 2001). For instance, the encircling of the DNA by eukaryotic DNA polymerase processivity factor PCNA (Krishna et al., 1994) and bacteriophage T4 gp45 (Moarefi et al., 2000) allows the polymerases to move rapidly without dissociation from the template. Similarly, the restriction–modification enzyme M.TaqI from *Thermus aquaticus* (Goedecke et al., 2001), the DNA restriction enzyme *Bam*HI (Viadiu & Aggarwal, 2000), and the TATA-box binding protein (TBP) (Chasman et al., 1993) all adopt a saddle conformation to slide along DNA for processive enzymatic or scanning actions. In this context, the substrate binding-induced conformational closure of the AMT complex may underpin its processive methylation along DNA (Beh et al., 2019; Wang et al., 2019). A detailed understanding of the enzymatic kinetics of the AMT complex awaits further investigation.

4 | LIMITATION OF THIS STUDY

Through introducing the DNA competitive inhibitor, OCR protein, we were able to capture the closed conformation of the AMT complex that is important for its substrate binding and methylation. This study therefore provides important insights into the AMT complex-mediated processive 6mA DNA methylation. However, the lack of defined density for OCR makes us unable to generate an accurate model for the AMT–OCR interaction. Furthermore, since the structure of the AMT–OCR complex is unable to provide insights into the base-specific AMT–DNA interactions in the active state, how the DNA substrate undergoes a transition from the encounter state to a productive methylation state remains uncharacterized. Future study on the productive state of the AMT–DNA complex is warranted for a detailed understanding of 6mA DNA methylation by the AMT complex.

5 | MATERIALS AND METHODS

5.1 | Plasmid

The genes for full-length *Tetrahymena thermophila* AMT1 and AMT7 were inserted in tandem into an in-house bacterial expression vector, in which AMT1 was preceded by an N-terminal His_6-MBP tag and a TEV cleavage site. Both DNA fragments encoding full-length *Tetrahymena thermophila* AMTP1 and AMTP2 were cloned into a modified pRSF-Duet vector preceded by an N-terminal His_6-SUMO tag and ULP1 (ubiquitin-like protease 1) cleavage site. The DNA fragment encoding *Escherichia* phage T7 OCR (residues 1–117; uniport number: P03775) was chemically synthesized by Integrated DNA Technologies and cloned into the pRSF-Duet vector.

5.2 | Protein expression and purification

The expression plasmids for AMT1, AMT7, and AMTP2 were co-transformed into BL21 (DE3) RIL cells strain (Agilent Technologies). The cells were initially grown at 37°C and were shifted to 16°C when OD_{600} reached 1.0. The cells were induced by the addition of 0.13 mM isopropyl β-D-1-thiogalactopyranoside (IPTG) and continued to grow overnight. The cells were lysed in buffer containing 50 mM Tris–HCl (pH 8.0), 1 M NaCl, 25 mM imidazole, 10% glycerol, 10 μg/mL DNase I, and 1 mM PMSF. The fusion proteins were purified using a Ni-NTA affinity column. The AMT1–AMT7–AMTP2 complex was then treated with ULP1 protease to remove the His_6-SUMO tag and TEV protease to remove the His_6-MBP tag, followed by ion-exchange chromatography on a HiTrap Heparin HP column (Cytiva) and size-exclusion chromatography on a HiLoad 16/600 Superdex 200 pg column (GE Healthcare) in 20 mM Tris–HCl (pH 7.5), 100 mM NaCl, 5% glycerol, and 5 mM DTT. Purified protein samples were stored at −80°C for further use.

The AMTP1 and OCR proteins were purified in a similar manner to the above, except that the cells were shifted to 16°C when OD_{600} reached 0.8. After cell lysis, the AMTP1 or OCR protein was purified using a Ni-NTA affinity column, followed by incubation with ULP1 protease to remove the His_6-SUMO tag. The AMTP1 protein was further purified by ion-exchange chromatography on a HiTrap Heparin HP column (Cytiva), and the OCR protein was purified using a HiTrap QHP Sepharose column (Cytiva). The tag-free AMTP1 or OCR protein was finally purified by size-exclusion chromatography on a HiLoad 16/600 Superdex 75 pg column (GE Healthcare) in 20 mM Tris–HCl (pH 7.5), 100 mM NaCl, 5% glycerol, and 5 mM DTT. Purified protein samples were stored at −80°C before use. The mutants of AMT1, AMT7, and AMTP1 were generated by site-directed mutagenesis and purified in the same manner as wild-type (WT) proteins.

5.3 | Radioactivity-based DNA methylation assay

To assess the OCR-mediated inhibition of the AMT complex, a synthesized 12-mer DNA duplex containing a single hemimethylated ApT site (upper strand:

5′-GCAAGXTCAACG-3′, X = 6-methyladenine; lower strand: 5′-CGTTGATCTTGC-3′) was used as DNA substrate. The 20-μL reaction mixture contained 1 μM AMT1–AMT7–AMTP1–AMTP2 complex, 1 μM DNA, and 0.56 μM S-adenosyl-L-[methyl-^{3}H] methionine with a specific activity of 18 Ci/mmol (PerkinElmer) in buffer containing 50 mM Tris–HCl (pH 8.0), 100 mM NaCl, 200 μg/mL BSA, 0.05% β-mercaptoethanol, and 5% glycerol in the presence or absence of 2 μM OCR. The reaction was performed at 30°C for 30 min before being quenched by 5 μL of 10 mM cold SAM. Eight microliters of the mixtures were loaded onto Hybond N nylon membrane (GE Healthcare) and dried out at room temperature, followed by washing with 0.2 M ammonium bicarbonate (pH 8.2) twice, deionized water once, and 95% ethanol once. The dry membrane was then transferred into a vial containing 3 mL of scintillation buffer (Fisher) and read by a Beckman LS6500 counter. The assays were performed in triplicate.

5.4 | Luminescence-based DNA methylation assay

For mutational analysis of the AMT complex, the MTase-Glo™ Methyltransferase Assay kit was used to detect activity (Promega). Specifically, 1 μM WT or mutant AMT complex was mixed with 10 μM SAM and the aforementioned hemimethylated 12-mer DNA duplex or unmethylated, self-complementary 24-mer DNA duplex (5′-CGCGATCGATGATCATC-GATCGCG-3′) in a buffer containing 20 mM Tris–HCl (pH 8.0), 50 mM NaCl, 1 mM EDTA, 3 mM $MgCl_2$, 100 μg/mL BSA, and 1 mM DTT at 30°C. The reaction lasted for 30 min before being quenched by 0.1% trifluoroacetic acid. Subsequently, the reaction mixture was first mixed with 2 μL 6× MTase-Glo™ reagent at room temperature for 30 min and then with 12 μL MTase-Glo™ detection solution for 30 min. The luminescence of the samples was measured in an opaque white 384-well microwell plate (Revvity) by CLARIOstar Plus (BMG LABTECH) at 25°C.

5.5 | Analytical size-exclusion chromatography

A 400-μL sample containing 18 μM AMT1–AMT7–AMTP1–AMTP2 complex, 36 μM OCR, or the AMT complex-OCR mixture was loaded onto a Superdex 200 increase 10/300 GL column (GE Healthcare) pre-equilibrated with 20 mM Tris–HCl (pH 7.5), 100 mM NaCl, 5% glycerol, and 5 mM DTT. The proteins in each of the elution fractions were visualized by SDS-PAGE imaging.

5.6 | Cryo-EM sample preparation and data collection

The concentration of the AMT1–AMT7–AMTP1–AMTP2–OCR complex was adjusted to 1.1 mg/mL in a buffer containing 20 mM Tris–HCl (pH 7.5), 100 mM NaCl, 5 mM DTT, and 2.5% Glycerol. Three microliters of the complex sample was applied to Quantifoil® (1.2/1.3) grids, which were glow discharged at 15 mA for 90 s. The grids were blotted for 7 s at 95% humidity with blot force 2 and plunge frozen using a Vitrobot Mark IV (Thermo Fisher).

The cryo-EM grids were imaged on a 300 keV Titan Krios cryo-electron microscope equipped with a K3 camera (Gatan) by the National Center for CryoEM Access and Training (NCCAT). Micrographs were collected at a magnification of ×81,000 with a super-resolution pixel size of 0.53 Å. The exposures were set with a total dose of ∼54 $e^-/Å^2$ over 50 frames and a defocus range of −0.4 to −3.1 μm.

5.7 | Cryo-EM data processing

In total 5,137 movies were processed using the CryoSPARC software package (v4.01) (Punjani et al., 2017). All movies are subject to 2 × 2 binning, patch motion correction, and patch-based contrast transfer function estimation. Subsequently, 2.6 million particles were picked using the Topaz program (Bepler et al., 2019) and extracted with a downscaled pixel size of 2.12 Å per pixel. After several rounds of 2D classification, 0.2 million particles were selected for 3D ab initio reconstruction and subsequent heterogeneous refinement. The particles with visible features of secondary and tertiary structures were re-extracted with a pixel size of 1.06 Å per pixel. The final set of particles was subject to the removal of duplicates and non-uniform refinement, resulting in a final resolution of 3.59 Å, as given by the Fourier shell correlation criterion (FSC 0.143).

5.8 | Model building and refinement

The structural model for AMT1–AMT7–AMTP2 complex was derived from that of the reported apo-state AMT complex (PDB 7YI8) (Yan et al., 2023). The structural models for AMTP1 and OCR were generated by the AlphaFold3 method (Abramson et al., 2024). Fitting the models into the density map was carried out using UCSF Chimera (v1.16) (Pettersen et al., 2004) and ChimeraX (v1.6.1) (Meng et al., 2023). The final structural model was obtained after iterative model building in Coot (v0.8.9.1) (Emsley et al., 2010), followed by real-space refinement in Phenix (Adams et al., 2010). In addition, the structural model for the AMT-bound

B-form DNA was generated and aligned with the density corresponding to the OCR protein in Coot.

AUTHOR CONTRIBUTIONS

Zengyu Shao: Data curation; visualization; validation; investigation; writing – original draft. **Sol Yoon:** Investigation. **Jiuwei Lu:** Investigation. **Pranav Athavale:** Investigation. **Yifan Liu:** Conceptualization; funding acquisition. **Jikui Song:** Conceptualization; supervision; project administration; writing – review and editing; funding acquisition.

ACKNOWLEDGMENTS

This work was supported by NIH grant (R35GM119721 to J.S.) and NSF award (MCB-2435178 to Y.L.). Cryo-EM data were collected at the National Center for CryoEM Access and Training (NCCAT) and the Simons Electron Microscopy Center located at the New York Structural Biology Center, supported by the NIH Common Fund Transformative High Resolution Cryo-Electron Microscopy program (U24 GM129539) and by grants from the Simons Foundation (SF349247) and NY State Assembly.

CONFLICT OF INTEREST STATEMENT

The authors declare no competing interest.

DATA AVAILABILITY STATEMENT

All data needed to evaluate the conclusions in the paper are present in the paper and/or the Supplementary Materials. Coordinates for the AMT1–AMT7–AMTP1–AMTP2–OCR complex have been deposited in the Protein Data Bank under accession codes 9O6K. The cryo-EM density map has been deposited to the EMDB under the accession numbers of EMD-70174.

ORCID

Jikui Song https://orcid.org/0000-0002-4958-1032

REFERENCES

Abramson J, Adler J, Dunger J, Evans R, Green T, Pritzel A, et al. Accurate structure prediction of biomolecular interactions with AlphaFold 3. Nature. 2024;630(8016):493–500.

Adams PD, Afonine PV, Bunkoczi G, Chen VB, Davis IW, Echols N, et al. PHENIX: a comprehensive Python-based system for macromolecular structure solution. Acta Crystallogr D Biol Crystallogr. 2010;66(Pt 2):213–21.

Beh LY, Debelouchina GT, Clay DM, Thompson RE, Lindblad KA, Hutton ER, et al. Identification of a DNA N6-adenine methyltransferase complex and its impact on chromatin organization. Cell. 2019;177(7):1781–1796.e1725.

Bepler T, Morin A, Rapp M, Brasch J, Shapiro L, Noble AJ, et al. Positive-unlabeled convolutional neural networks for particle picking in cryo-electron micrographs. Nat Methods. 2019;16(11):1153–60.

Bird AP, Wolffe AP. Methylation-induced repression—belts, braces, and chromatin. Cell. 1999;99(5):451–4.

Boulias K, Greer EL. Means, mechanisms and consequences of adenine methylation in DNA. Nat Rev Genet. 2022;23(7):411–28.

Bourc'his D, Bestor TH. Meiotic catastrophe and retrotransposon reactivation in male germ cells lacking Dnmt3L. Nature. 2004;431(7004):96–9.

Breyer WA, Matthews BW. A structural basis for processivity. Protein Sci. 2001;10(9):1699–711.

Burglin TR, Affolter M. Homeodomain proteins: an update. Chromosoma. 2016;125(3):497–521.

Chasman DI, Flaherty KM, Sharp PA, Kornberg RD. Crystal structure of yeast TATA-binding protein and model for interaction with DNA. Proc Natl Acad Sci U S A. 1993;90(17):8174–8.

Chen J, Hu R, Chen Y, Lin X, Xiang W, Chen H, et al. Structural basis for MTA1c-mediated DNA N6-adenine methylation. Nat Commun. 2022;13(1):3257.

Cheng X. DNA modification by methyltransferases. Curr Opin Struct Biol. 1995a;5(1):4–10.

Cheng X. Structure and function of DNA methyltransferases. Annu Rev Biophys Biomol Struct. 1995b;24:293–318.

Du Q, Luu PL, Stirzaker C, Clark SJ. Methyl-CpG-binding domain proteins: readers of the epigenome. Epigenomics. 2015;7(6):1051–73.

Emsley P, Lohkamp B, Scott WG, Cowtan K. Features and development of Coot. Acta Crystallogr D Biol Crystallogr. 2010;66(Pt 4):486–501.

Feng X, He C. Mammalian DNA N(6)-methyladenosine: challenges and new insights. Mol Cell. 2023;83(3):343–51.

Fraenkel E, Pabo CO. Comparison of X-ray and NMR structures for the antennapedia homeodomain-DNA complex. Nat Struct Biol. 1998;5(8):692–7.

Fu Y, Luo GZ, Chen K, Deng X, Yu M, Han D, et al. N6-methyldeoxyadenosine marks active transcription start sites in Chlamydomonas. Cell. 2015;161(4):879–92.

Goedecke K, Pignot M, Goody RS, Scheidig AJ, Weinhold E. Structure of the N6-adenine DNA methyltransferase M.TaqI in complex with DNA and a cofactor analog. Nat Struct Biol. 2001;8(2):121–5.

Gupta YK, Chan SH, Xu SY, Aggarwal AK. Structural basis of asymmetric DNA methylation and ATP-triggered long-range diffusion by EcoP15I. Nat Commun. 2015;6:7363.

Holm L, Rosenstrom P. Dali server: conservation mapping in 3D. Nucleic Acids Res. 2010;38:W545–9.

Horton JR, Woodcock CB, Opot SB, Reich NO, Zhang X, Cheng X. The cell cycle-regulated DNA adenine methyltransferase CcrM opens a bubble at its DNA recognition site. Nat Commun. 2019;10(1):4600.

Issinger OG, Hausmann R. Synthesis of phage coded products during infection of E. coli in gene-1-mutants of phages T3 and T7. Hoppe Seylers Z Physiol Chem. 1972;353(10):1530.

Jones PA, Gonzalgo ML. Altered DNA methylation and genome instability: a new pathway to cancer? Proc Natl Acad Sci U S A. 1997;94(6):2103–5.

Krishna TS, Kong XP, Gary S, Burgers PM, Kuriyan J. Crystal structure of the eukaryotic DNA polymerase processivity factor PCNA. Cell. 1994;79(7):1233–43.

Law JA, Jacobsen SE. Establishing, maintaining and modifying DNA methylation patterns in plants and animals. Nat Rev Genet. 2010;11(3):204–20.

Lee JK, Bosnakovski D, Toso EA, Dinh T, Banerjee S, Bohl TE, et al. Crystal structure of the double homeodomain of DUX4 in complex with DNA. Cell Rep. 2018;25(11):2955–2962.e2953.

Li S, Xu T, Meng X, Yan Y, Zhou Y, Duan L, et al. OCR-mediated suppression of BrxX unveils a phage counter-defense mechanism. Nucleic Acids Res. 2024;52(14):8580–94.

Luo GZ, Blanco MA, Greer EL, He C, Shi Y. DNA N(6)-methyladenine: a new epigenetic mark in eukaryotes? Nat Rev Mol Cell Biol. 2015;16(12):705–10.

Meng EC, Goddard TD, Pettersen EF, Couch GS, Pearson ZJ, Morris JH, et al. UCSF ChimeraX: tools for structure building and analysis. Protein Sci. 2023;32(11):e4792.

Moarefi I, Jeruzalmi D, Turner J, O'Donnell M, Kuriyan J. Crystal structure of the DNA polymerase processivity factor of T4 bacteriophage. J Mol Biol. 2000;296(5):1215–23.
Mondo SJ, Dannebaum RO, Kuo RC, Louie KB, Bewick AJ, LaButti K, et al. Widespread adenine N6-methylation of active genes in fungi. Nat Genet. 2017;49(6):964–8.
Padmanaban S, Lambacher NJ, Tesmer VM, Zhang J, Shibuya H, Nandakumar J. Caenorhabditis elegans telomere-binding proteins TEBP-1 and TEBP-2 adapt the Myb module to dimerize and bind telomeric DNA. Proc Natl Acad Sci U S A. 2024; 121(16):e2316651121.
Panning B, Jaenisch R. RNA and the epigenetic regulation of X chromosome inactivation. Cell. 1998;93(3):305–8.
Pettersen EF, Goddard TD, Huang CC, Couch GS, Greenblatt DM, Meng EC, et al. UCSF chimera—a visualization system for exploratory research and analysis. J Comput Chem. 2004; 25(13):1605–12.
Punjani A, Rubinstein JL, Fleet DJ, Brubaker MA. cryoSPARC: algorithms for rapid unsupervised cryo-EM structure determination. Nat Methods. 2017;14(3):290–6.
Putnam CD, Tainer JA. Protein mimicry of DNA and pathway regulation. DNA Repair (Amst). 2005;4(12):1410–20.
Razin A, Riggs AD. DNA methylation and gene function. Science. 1980;210(4470):604–10.
Ren W, Gao L, Song J. Structural basis of DNMT1 and DNMT3A-mediated DNA methylation. Genes (Basel). 2018;9(12):620.
Sheng Y, Wang Y, Yang W, Wang XQ, Lu J, Pan B, et al. Semiconservative transmission of DNA N (6)-adenine methylation in a unicellular eukaryote. Genome Res. 2024;34(5):740–56.
Shi Z, He F, Chen M, Hua L, Wang W, Jiao S, et al. DNA-binding mechanism of the Hippo pathway transcription factor TEAD4. Oncogene. 2017;36(30):4362–9.
Sledz P, Jinek M. Structural insights into the molecular mechanism of the m(6)A writer complex. Elife. 2016;5:e18434.
Song J, Pfeifer GP. Are there specific readers of oxidized 5-methylcytosine bases? Bioessays. 2016;38(10):1038–47.
Viadiu H, Aggarwal AK. Structure of BamHI bound to nonspecific DNA: a model for DNA sliding. Mol Cell. 2000;5(5):889–95.
Walkinshaw MD, Taylor P, Sturrock SS, Atanasiu C, Berge T, Henderson RM, et al. Structure of OCR from bacteriophage T7, a protein that mimics B-form DNA. Mol Cell. 2002;9(1):187–94.
Walsh CP, Chaillet JR, Bestor TH. Transcription of IAP endogenous retroviruses is constrained by cytosine methylation. Nat Genet. 1998;20(2):116–7.
Wang P, Doxtader KA, Nam Y. Structural basis for cooperative function of Mettl3 and Mettl14 methyltransferases. Mol Cell. 2016; 63(2):306–17.
Wang X, Feng J, Xue Y, Guan Z, Zhang D, Liu Z, et al. Structural basis of N(6)-adenosine methylation by the METTL3-METTL14 complex. Nature. 2016;534(7608):575–8.
Wang Y, Nan B, Ye F, Zhang Z, Yang W, Pan B, et al. Dual modes of DNA N(6)-methyladenine maintenance by distinct methyltransferase complexes. Proc Natl Acad Sci U S A. 2025;122(3): e2413037121.
Wang Y, Sheng Y, Liu Y, Zhang W, Cheng T, Duan L, et al. A distinct class of eukaryotic MT-A70 methyltransferases maintain symmetric DNA N6-adenine methylation at the ApT dinucleotides as an epigenetic mark associated with transcription. Nucleic Acids Res. 2019;47(22):11771–89.
Yan J, Liu F, Guan Z, Yan X, Jin X, Wang Q, et al. Structural insights into DNA N(6)-adenine methylation by the MTA1 complex. Cell Discov. 2023;9(1):8.
Zhang X, Zhang Y, Wang C, Wang X. TET (ten-eleven translocation) family proteins: structure, biological functions and applications. Signal Transduct Target Ther. 2023;8(1):297.

SUPPORTING INFORMATION

Additional supporting information can be found online in the Supporting Information section at the end of this article.

How to cite this article: Shao Z, Yoon S, Lu J, Athavale P, Liu Y, Song J. Structural insight into the substrate binding of the AMT complex via an inhibitor-trapped state. Protein Science. 2025; 34(9):e70265. https://doi.org/10.1002/pro.70265